ARTICLE

Experimental Realization of Subradiant, Superradiant, and Fano Resonances in Ring/Disk Plasmonic Nanocavities

Yannick Sonnefraud,[†,#] Niels Verellen,[‡,§,⊥,#] Heidar Sobhani,[¶] Guy A.E. Vandenbosch,[⊥] Victor V. Moshchalkov,[§] Pol Van Dorpe,[‡,*] Peter Nordlander,[¶,*] and Stefan A. Maier[†,*]

[†]Experimental Solid State Group, Physics Department, Imperial College London, London SW7 2AZ, U.K., [‡]IMEC, Kapeldreef 75, 3001 Leuven, Belgium, [§]INPAC-Institute for Nanoscale Physics and Chemistry, Nanoscale Superconductivity and Magnetism and Pulsed Fields Group, K. U. Leuven Celestijnenlaan 200 D, B-3001 Leuven, Belgium, [⊥]ESAT-TELEMIC, K. U. Leuven, B-3001 Leuven, Belgium, and [¶]Laboratory for Nanophotonics, Department of Physics and Astronomy, M.S. 61, Rice University, Houston, Texas 77005-1892. [#]These authors contributed equally.

ABSTRACT Subradiant and superradiant plasmon modes in concentric ring/disk nanocavities are experimentally observed. The subradiance is obtained through an overall reduction of the total dipole moment of the hybridized mode due to antisymmetric coupling of the dipole moments of the parent plasmons. Multiple Fano resonances appear within the superradiant continuum when structural symmetry is broken *via* a nanometric displacement of the disk, due to coupling with higher order ring modes. Both subradiant modes and Fano resonances exhibit substantial reductions in line width compared to the parent plasmon resonances, opening up possibilities in optical and near IR sensing *via* plasmon line shape design.

KEYWORDS: plasmonics · optical nanocavities · Fano resonance · subradiance · superradiance

Localized plasmon resonances in small metallic nanostructures have attracted large interest in the scientific community for over a century because of their strong interaction with visible light.[1,2] Initially, studies focused mainly on colloidal particles but more recently, along with the development of the field of nanoplasmonics, more insight and control has been gained on localized plasmon resonances in well-controlled structures fabricated using top-down nanotechnology.[3,4] It is well-known that the electromagnetic field in the vicinity of a nanoparticle is enhanced at the plasmon resonance. This enhanced near field can be used to increase the sensitivity of various spectroscopic techniques, such as Raman scattering or infrared absorption spectroscopy.[5−7] Moreover, the scattering and absorption cross sections of nanoparticles are enhanced at the plasmon resonance, which can be used to increase the efficiency of solar cells,[8] or possibly cure cancer utilizing thermal effects.[9] As the spectral position of the plasmon resonance depends on the refractive index of the medium surrounding the nanoparticle, nanoplasmonic structures can also be utilized as highly integrated optical sensors.[10]

All the above-mentioned applications use the fact that the plasmon resonance depends directly on the morphology and size of the nanoparticle. Various geometries have been proposed and fabricated to match the requirements of the application, ranging from spheres,[1,11] rods,[11] or rings[12,13] to more complex structures such as nanoeggs or nanostars.[14,15] Control over the spectral position of the plasmon resonance in such *single* nanostructures is generally very good. However, control over the line shape of the resonance has not yet received as much attention, although many applications would benefit from for example nanostructures with sharp plasmon resonances, that is, a higher quality factor. For instance, Sherry and co-workers have introduced the concept of a figure of merit (FOM) to characterize the sensitivity of a plasmonic sensor:[16] this FOM is inversely proportional to the width of the resonance. Another example is the "spaser":[17] the production of a coherent output of surface plasmons or photons in plasmonic nanocavities, which will also require a high quality factor.

The main decay channels contributing to the line width of a plasmon resonance are nonradiative decay of the coherent electron oscillations in internal channels (inter/intra-band transitions of the electrons, interaction with phonons, *etc.*), and radiative decay.[18,19] For small particles (diameter $\ll \lambda_{res}$), nonradiative processes are dominating.[11,19] For larger particles (diameter $> \lambda_{res}$), radiative damping dominates.[20] To manipulate the radiative damping, one

*Address correspondence to pvandorp@imec.be, nordland@rice.edu, s.maier@imperial.ac.uk.

Received for review November 7, 2009 and accepted February 4, 2010.

Published online February 15, 2010. 10.1021/nn901580r

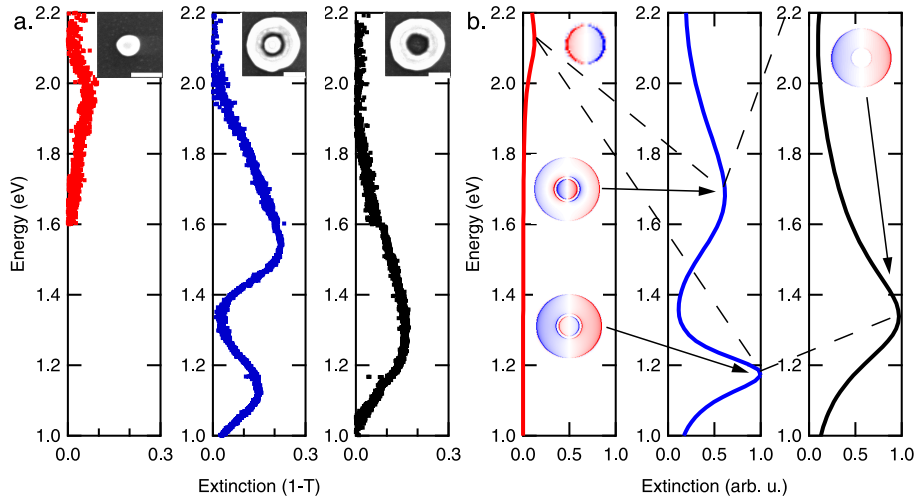

Figure 1. Hybridization diagram for a concentric ring/disk cavity (CRDC). (a) Experimental extinction measurements of single structures, a disk (red), CRDC (blue) and ring (black). D_{out} = 250 nm, D_{in} = 100 nm, $D_{disk} \approx$ 75 nm. The insets show scanning electron microscopy (SEM) images of the structures, with a scale bar of 100 nm. (b) Simulated extinction curves for the structures of panel a for D_{out} = 250 nm, D_{in} = 100 nm, D_{disk} = 92 nm and a thickness of 60 nm. The insets show the charge densities for the respective resonances, blue (respectively red) indicating negative (respectively positive) charges.

can exploit the concept of plasmon hybridization[21] to study coherent coupling between closely spaced nanostructures. For example, it has been predicted theoretically that concentric ring/disk cavities (CRDC) will exhibit sub- and superradiant modes due to hybridization of the fundamental dipolar modes of the two constituents,[22] and that Fano resonances can arise due to the interaction with higher order modes, when the structural symmetry is broken.[23] Coherent effects in plasmonic nanocavities and particularly Fano resonances have recently received a large amount of attention.[23−32] The Fano resonance can evolve into a classical analogue of electromagnetically induced transparency (EIT) when the energy levels of the interacting resonances coincide.[30,33,34]

In this letter we focus on a first experimental characterization of sub- and superradiant plasmonic modes, as well as Fano resonances, in ring/disk nanocavities. Using confocal spectroscopy of single cavities, we experimentally demonstrate that a CRDC exhibits both subradiant and superradiant dipolar modes, as suggested by earlier simulations.[22] Moreover, by displacing the disk from the center of the ring in a nonconcentric ring/disk cavity (NCRDC) we observe the coherent interaction between the bright dipolar resonances of the disk and the dark multipolar resonances of the ring, which generates Fano resonances. We also comment on the sensing capacities of these structures. The experimental results are well supported by finite-difference time-domain (FDTD) simulations, which shed light on the nature of the underlying resonances.

RESULTS AND DISCUSSION

Figure 1 presents a hybridization diagram outlining how the sub- and superradiant dipolar modes arise from the associated parent plasmon modes in a CRDC with outer ring diameter D_{out} = 250 nm, inner ring diameter D_{in} = 100 nm, disk diameter $D_{disk} \approx$ 75 nm and thickness 50 nm. Figure 1a shows the experimentally measured extinction and Figure 1b the corresponding curves obtained *via* FDTD. The extinction of the ring alone (black curve) exhibits a peak in the near-infrared, corresponding to a dipolar mode, as shown by the charge plot in the inset. If a disk with a diameter D_{disk} slightly smaller than D_{in} is inserted at the center of the ring, its dipolar mode (red curve) hybridizes with the dipolar ring modes as indicated by the dotted lines, giving rise to the observed extinction spectrum of a CRDC (blue curves). The dipolar mode at higher energies exhibits an increased line width and has acquired a superradiant character due to a parallel coupling between the dipolar modes of the parent disk and ring plasmons. Conversely, in the low energy mode, an antiparallel orientation of the parent dipole moments leads to a reduced net dipole moment. This subradiant character is reflected in the spectrally sharper line width with smaller radiative losses. This interpretation is well supported by the surface charge plots at the associated resonance energies, depicted in the insets.

To experimentally obtain the true resonance line width, problems induced by chromatic aberrations at low energies had to be circumvented. We therefore performed separate measurements, employing illumination by short wavelength intervals at a time (not shown). These measurements show experimental full width at half-maximum linewidths of 680 ± 50 meV for the ring dipole, and 330 ± 50 meV for the subradiant mode of a CRDC with an estimated gap of 6 nm. For these device parameters, simulations have indicated linewidths of 350 ± 10 meV for the ring and 130 ± 10 meV for the CRDC. One will note that in this study, the simulated linewidths are systematically lower than the

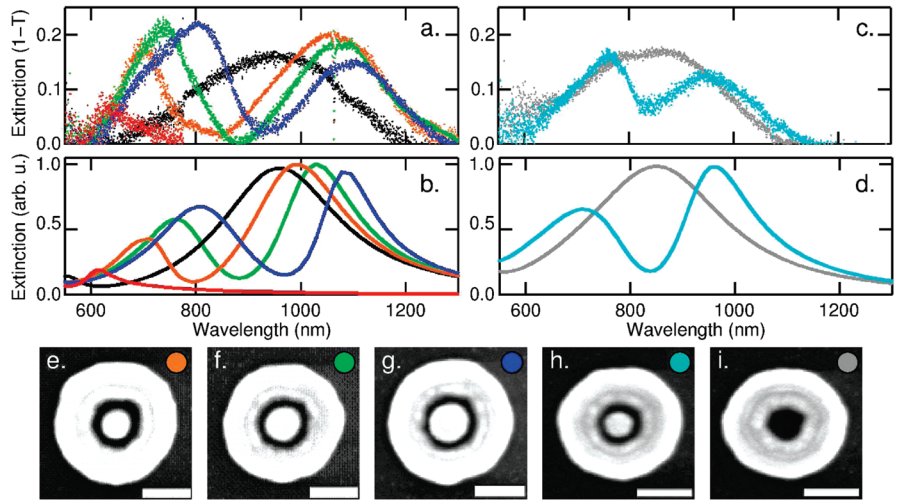

Figure 2. Evolution of the CRDC extinction with varying gap size, and ring size. (a) Measured extinction spectra of single structures. The black, red, and blue curves show the extinction of the particular ring, disk, and CRDC presented in Figure 1, corresponding to the image in panel g with $D_{disk} \approx 75$ nm. The orange and green curves show the extinction for smaller disk sizes, shown in the SEM images in panels e and f. (b) Simulated extinction cross sections, with ring-disk gap of 8, 6, and 4 nm for the orange, green, and blue curves, respectively. (c) Measured extinction spectra for a smaller ring with dimensions $D_{out} = 220$ nm, $D_{in} = 75$ nm (gray curve, SEM image shown in panel i) and a corresponding CRDC with a disk of $D_{disk} \approx 66$ nm inserted into that ring (light blue curve, SEM image h.). (d) Simulated extinction cross sections for the cavities of panel c. (e−i) SEM images of CRDCs and ring. Scale bars: 100 nm.

experimental linewidths. We attribute this to the fact that in the simulations, the dielectric constant used to simulate the gold is a bulk dielectric constant. The fabricated structures present a high surface over volume ratio, which deviates from a bulk approximation. Moreover, the walls of the structures are rough, because of the fabrication process used here. This can be observed on the SEM images presented in this report. For this reason, the gap size is not constant within one device, causing some inhomogenous broadening within one nanostructure. Those two effects contribute to the increase of the losses in the structures, leading to linewidths larger in the experiment than in the simulations.

This concentric arrangement allows for a formidable control over the plasmon resonance position and width of the structure. Indeed, as it is the case for any plasmonic resonator, one can select the spectral position of the resonances by changing its dimensions. This is illustrated on Figure 2: panel a (respectively c) presents the experimental extinction cross sections for cavities built out of a ring with dimensions $D_{out} = 250$ nm, $D_{in} = 100$ nm (respectively $D_{out} = 220$ nm, $D_{in} = 75$ nm). The corresponding FDTD simulations are shown in panels b and d. One can observe that the 30 nm reduction in the diameter of the ring leads to a 100 nm blue-shift of the resonances. In addition, the line width tuning, for a specific ring, of the corresponding CRDC can be achieved by varying the gap between ring and disk. The smaller the gap is, the stronger is the interaction between ring and disk modes, leading also to an increase in the spectral separation of the sub- and superradiant modes. Figure 2 panels a and b illustrate this effect for the same ring as in Figure 1. In the experimental structures (SEM images shown in Figure 2e−g; measured extinction spectra in Figure 2a), the target gap is changed by steps of 2.5 nm. The gap obtained at the end of the fabrication process is difficult to estimate, as shown on the SEM images. In the simulations (Figure 2b), the gaps are 8, 6, and 4 nm. Both measured and simulated extinctions clearly show how the subradiant mode shifts toward the red and narrows as the gap is reduced, with widths of 190 ± 10, 140 ± 10, and 90 ± 10 meV for gaps of 8, 6, and 4 nm, respectively. This additional degree of freedom for the plasmon resonance can be of interest for many applications. We will discuss two of them, surface enhanced raman scattering (SERS) and sensing, in a later part of this report.

Another route to produce pronounced sharp features in plasmon resonances is the use of dark modes. Those modes take their name from the fact that the symmetry of their charge distribution forbids a direct coupling to photons in the nonretarded case. Their radiative losses are therefore highly reduced, leading to an intrinsically sharper line shape compared to bright modes. Indirect excitation of dark modes can be enabled *via* the breaking of the structural symmetry of the unit, as we will now show. This way, a bright mode of a cavity can exert a moment on a dark mode and hence excite it. The spectrum of the hybridized structure then shows a Fano resonance, i.e. an interference pattern between the bright and dark mode: a dip is created in the broad bright resonance.

Figure 3 shows this effect for a specific NCRDC made out of a ring with the parameters $D_{out} = 350$ nm and $D_{in} = 200$ nm and a disk of diameter $D_{disk} = 150$ nm, and Figure 4 presents the charge plots associated with the different resonances involved in this NCRDC, both figures sharing the same color conventions. Figure 3 pan-

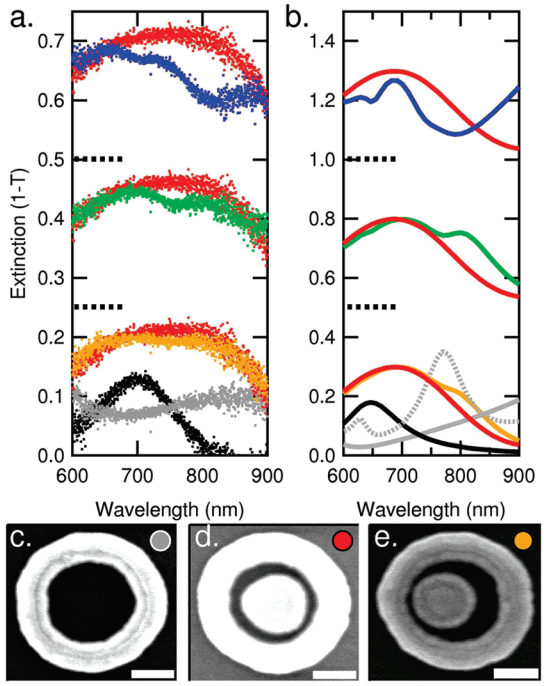

Figure 3. Fano resonances in nonconcentric ring/disk cavities (NCRDC). (a) Measured extinction spectra of single cavities with various degrees of broken structural symmetry. Black, disk with D_{disk} = 150 nm; gray, ring with D_{out} = 350 nm and D_{in} = 200 nm; red, concentric combination of both; orange, green, and blue, nonconcentric arrangements with increasing offsets. (b) Corresponding simulated extinction cross sections. Color code identical to panel a, but gray (respectively, dotted gray): ring illuminated at normal (respectively, grazing) incidence. Orange, green, and blue curves are for structures with gaps of 12, 8, and −4 nm, respectively. Spectra have been offset for clarity, the dotted lines giving their baselines. (c−e) SEM images of the corresponding ring (gray curves), CRDC (red curves), and NCRDC (orange curves). Scale bars: 100 nm.

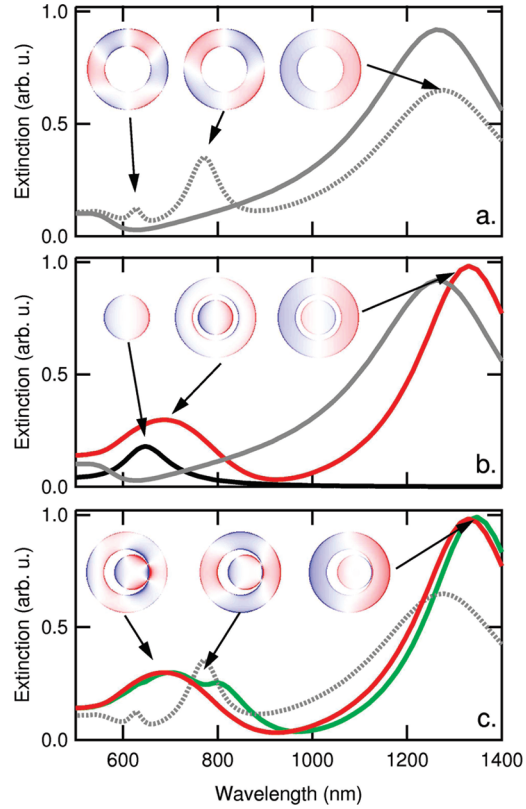

Figure 4. Charge plots and extinction cross sections for cavities formed by combining a disk of D_{disk} = 150 nm and a ring with D_{out} = 350 nm and D_{in} = 200 nm. For each charge plot, blue (respectively, red) indicates a negative (respectively, positive) charge value. (a) Extinction cross sections of a ring only, illumination at normal incidence (gray) or grazing incidence (dotted gray). The insets display the charge distribution in the ring. (b) Disk (black), ring (gray), and CRDC (red). Insets (left to right): dipole mode of the disk, superradiant and subradiant modes of the CRDC. (c) Ring at grazing incidence (dotted gray), CRDC (red), and NCRDC (green) with a gap of 8 nm. Insets (left to right): Fano resonance from the octupole mode of the ring, Fano resonance from the quadrupole, and subradiant mode, all in the NCRDC.

els a and b show extinction spectra obtained from measurements and simulations, respectively, with different degrees of symmetry breaking. Figure 3 panels c, d, and e show representative SEM images of the ring, CRDC, and NCRDC. As apparent from the extinction spectrum obtained using oblique incidence (gray dotted line in Figure 3b), the ring cavity exhibits a series of higher order, dark modes at energies within the superradiant continuum, which are not directly excited at normal incidence (gray solid line). The insets in 4a present the charge distributions associated with those high order modes, illustrating their symmetry: the lowest wavelength peak is an octupole mode, and the peak just below 800 nm is a quadrupole mode.

When the symmetry of the CRDC is broken by displacing the disk from the center of the ring (*cf.* Figure 3e and Figure 4c), these dark ring modes can interact with the superradiant mode. Hence, a change in line shape occurs from that of the concentric case (red curve) to a situation where dips in extinction are apparent, with a depth increasing with increasing offset of the disk from the ring center (Figure 3, orange and green curves). The interaction gets even stronger when the disk starts to touch the ring (blue curve). The experimental trend follows very well the simulations, apart from a slight red-shift of a few tens of nanometers. The Fano resonance represents a narrow spectral transmission band within the broad continuum with a line width around 150 ± 20 meV, which is less than half of the 370 ± 20 meV line width of the disk alone. One can note from the charge plots in 4c that, at the wavelengths corresponding to the Fano interferences, the charge distribution in the disk is not purely dipolar anymore. A quadrupolar component appears, induced by the charge symmetry in the ring.

Apart from fundamental interest in these coherent processes, which utilizes plasmonic nanostructures as model systems for classical oscillator physics, the radiative line width tuning they enable can be applied in various situations. We will discuss two of them: SERS enhancement and plasmonic sensing. In SERS, the enhancement of the Raman signal of an analyte is linked to the field intensity at the position of this analyte,[35] or

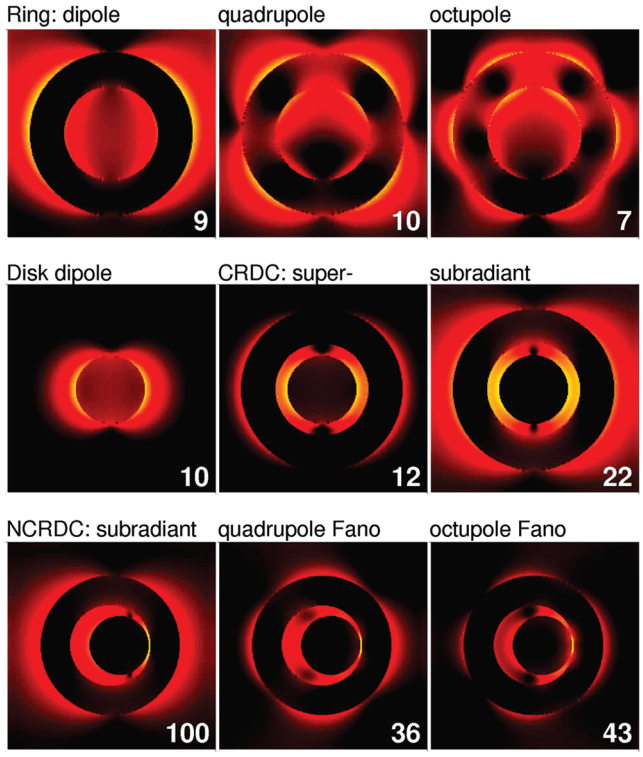

Figure 5. Field plots ($|\tilde{E}|$) at the indicated resonances for cavities made out of a combination of a disk with D_{disk} = 150 nm and a ring with D_{out} = 350 nm and D_{in} = 200 nm, extracted from FDTD simulations. In the case of the NCRDC, the gap is 8 nm. The cut plane is parallel to the interface substrate/cavity, three mesh cells above the interface. The white number indicates the maximum field enhancement. The colorscale used is logarithmic, ranging from a field of 1 (no enhancement) to the maximum value.

more specifically, in the case of a plasmonic cavity, to the ratio between the quality factor of the cavity Q and the effective mode volume V_{eff} of the field at the position of the analyte.[36] To illustrate how CRDC and NCRDC can be of use in this context, let us consider the case of cavities made out of a disk with D_{disk} = 150 nm and a ring with D_{out} = 350 nm and D_{in} = 200 nm. These dimensions correspond to those of the structures discussed in Figure 3 and Figure 4. Figure 5 shows how the electric field is confined in the gaps between ring and disk, and that such structures can lead to enhancements of more than 2 orders of magnitude in the case where the symmetry is broken. From the values of the field, one can extract the effective mode volume experienced by an analyte sitting at the position of highest field in those cavities, or at the center of the gap. Table 1 summarizes the effective mode volume normalized to $(\lambda/2)^3$, $\tilde{V}_{eff}$, the quality factor Q of the resonance, and the ratio of these two values $Q/\tilde{V}_{eff}$. The details of the calculation of the effective mode volume can be found in the Methods section. The quality factors are obtained by fitting the simulated extinction curves to Lorentzian functions to estimate the full width half-maximum of the resonance.

TABLE 1. Normalized Effective Mode Volume ($\tilde{V}_{eff} = V_{eff}/(\lambda/2)^3$) for Different Modes of Cavities Made from a Disk with D_{disk} = 150 nm and a Ring with D_{out} = 350 nm and D_{in} = 200 nm (NCRDC Has a Gap of 8 nm)

mode	$\tilde{V}_{eff}$	Q	$Q/\tilde{V}_{eff}$
ring dipole	2.7×10^{-2}	4.2	1.6×10^{2}
disk dipole	4.3×10^{-2}	4.7	1.1×10^{2}
CRDC subradiant	1.2×10^{-2}	5.1	4.3×10^{2}
NCRDC subradiant	1.8×10^{-3}	5.2	2.9×10^{3}

As one can see from the table, for all the situations, the field is confined on scales much smaller than what is possible in a normal diffraction-limited cavity. Moreover, $\tilde{V}_{eff}$ is several times smaller for all the cavities involving a ring compared to a simple disk. Eventually, breaking the symmetry allows for nearly 1 order of magnitude increase in the ratio $Q/\tilde{V}_{eff}$ from the CRDC to the NCRDC, and more than 1 order of magnitude compared to the bare ring. Those last figures are representative of the enhancement gain expected in SERS. Note that the discussion here is focused on cavities presenting dimensions which are accessible for fabrication: the gap in the NCRDC is 8 nm, and 25 nm in the CRDC. Reducing the gap size would accordingly reduce the effective mode volume.

We finish our discussion by a preliminary sensing study where the whole structure is immersed in liquid. Figure 6a shows how the resonance of the structure described in Figure 1a (blue curves) behaves in media with different refractive indices. The experiment has been conducted by creating a small "cell" with the substrate and a second glass slide, separated by optical fibres, as sketched in panel c. Water is introduced in the cell after treating the sample in an O_2 plasma cleaner (50 W, 3 min) to improve wetting of the surface, and the spectra are acquired (blue curve in 4a). They are then compared with the spectra for the cell

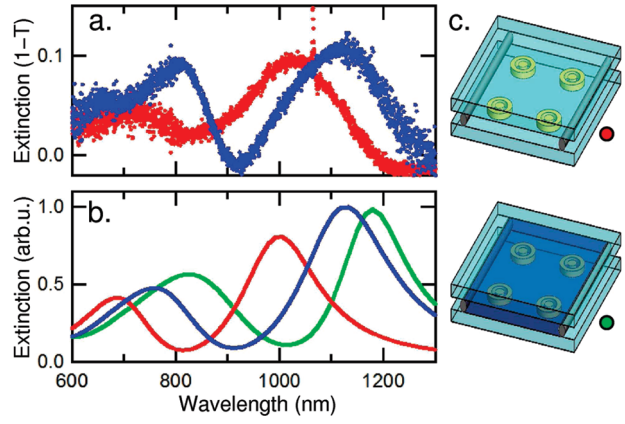

Figure 6. Sensing with a CRDC. (a) Experimental extinction spectra for the cavity (dimensions D_{out} = 250 nm, D_{in} = 100 nm, and $D_{disk} \approx$ 75 nm) in air (red) and water (blue). (b) Simulated spectra for a similar cavity (D_{out} = 248 nm, D_{in} = 100 nm, and D_{disk} = 88 nm). Red, in air; green, in water, with the gap completely filled; and blue, in water with $^3/_4$ of the gap filled. (c) Sketches of the sensing cell: optical fibres (diameter $\approx$ 200 μm) separate the sample from a capping glass coverslip.

filled with air (red curves). In the experiment a red-shift of 90 ± 10 nm of the low-energy peak is observed (*i.e.*, 510 meV RIU^{-1}), which would correspond to a FOM[37] of 1.6. Turning our attention to the corresponding simulations (Figure 6b), we observe that the expected shift should be 175 nm for a similar refractive index change (600 meV RIU^{-1}, FOM of 3, red curve to green curve). The discrepancy can be explained by the fact that most of the sensing capabilities of the cavities lie in the gap,[22,23] where the water wetting is very poor. This reduces the observed shift compared to total filling. For instance, a simulation accounting for a filling of only $^3/_4$ of the gap height seems to reproduce very well the experimental shift (Figure 6b, green curve). Although higher FOMs for single nanostructures have indeed been reported in the literature (up to 5.4 for silver nanoparticles with resonances in the visible part of the spectrum,[38,37] or 3.8 in a gold planar metamaterial in the IR[39]), our approach allows for radiative loss and hence FOM engineering throughout the whole near-IR and, *via* scaling, also the mid-IR part of the spectrum, where resonances of single nanostructures show large radiative damping due to their physical size. Further optimization of cavity fabrication should allow to create structures with higher FOMs.[23]

CONCLUSIONS

We have reported experimental demonstrations of hybridized subradiant, superradiant, and Fano-type modes in ring/disk plasmonic nanocavities. For the subradiant mode, the line width is reduced by more than a factor of 2 compared to the parent ring and disk modes. By breaking the symmetry of the structure narrow Fano resonances are induced. Our investigations show that radiative lifetime tuning of hybridized nanocavity modes is a promising path for the development of plasmonic substrates for chemical sensing, biosensing, and SERS.

METHODS

Gold nanocavities were fabricated on thin glass slides (~0.15 mm thick) coated with 10 nm ITO. After sputtering a nominally 50 nm Au/4 nm Ag film an etch mask was created by electron-beam lithography using a negative-tone hydrogen silsesquioxane (HSQ) resist coating. By means of Xe ion milling the mask was then transferred into the Au layer resulting in the final cavities. The residual etch mask layer on top of the particles behaves optically as silicon dioxide and is not removed. Moreover, as a consequence of the etching process, the particles' sidewalls are slanted with an angle of approximately 20 degrees. To enable single particle spectroscopy, the cavities are arranged on a grid with a pitch of 4 μm, so that only one cavity lies in the focal region of the confocal microscope.

Electromagnetic modeling was performed using the FDTD method. The dielectric response of the metal was fitted to the experimentally determined dielectric permittivity using a combination of Drude and Lorentz oscillator terms.[40] This fit has excellent agreement with the dielectric permittivity of the particular Au films obtained in our fabrication process from 600 nm onward, as confirmed *via* ellipsometry. The effect of the glass substrate (refractive index of 1.5) on the resonances has been taken into account in the simulations and leads to a red-shift with respect to extinction calculations in vacuum. Also the slanted sidewalls are taken into account, the effect of the capping resist layer is not. All the charge plots are calculated at the top surface of the structures.

We define the effective mode volume V_{eff} by analogy with the effective mode lengths discussed in ref 36. To do so, we use u_E, the electromagnetic energy density at the point of coordinate *r*. For lossy metals,

$$u_E = \frac{\varepsilon_0}{2}\left(\varepsilon_1 + \frac{2\omega\varepsilon_2}{\gamma}\right)|\mathbf{E}|^2 \qquad (1)$$

where $\varepsilon(\omega) = \varepsilon_1(\omega) + i\varepsilon_2(\omega)$ is the complex dielectric function of a Drude model with damping γ. Then

$$V_{eff}(\mathbf{r}_0)\, u_E(\mathbf{r}_0) = \int u_E(\mathbf{r})\, d\mathbf{r} \qquad (2)$$

where $\mathbf{r}_0$ is the position of an analyte. In the case of a ring or a disk, $\mathbf{r}_0$ is two mesh cells (4 nm) away from the structure, in the direction giving the highest field. In the case of CRDC, $\mathbf{r}_0$ is in the gap, 4 nm away from the disk, in the direction of the incident polarization. In the case of NCRDC, $\mathbf{r}_0$ is at the center of the gap. Those positions are chosen to avoid unphysical field values due to stair casing effect.

The confocal acquisition of the spectra is described in detail elsewhere.[30] Briefly, the radiation of a white light supercontinuum is polarized and then focused on the sample with a 10× microscope objective. The light transmitted through the sample is collected by a 50× IR-corrected microscope objective and spatially filtered by the entrance of an optical fiber in order to select only the signal coming from the focal region. The signal is then guided *via* the fiber to the detectors, a silicon CCD and APD for energies higher than 1.6 eV, and InGaAs below.

Acknowledgment. S.A.M. and Y.S. acknowledge support by the U.K. Engineering and Physical Sciences Research Council. N.V. acknowledges support from IMEC and the Methusalem funding by the Flemish Government. P.V.D. acknowledges financial support from the F.W.O. (Flanders). H.S., and P.N. acknowledge support from the U.S. Army Research Laboratory and the U.S. Army Research Office under Grant W911NF-04-1-0203, the Robert A. Welch Foundation under Grant C-1222, and NSF under Grant CNS-0421109. We thank Jos Moonens for e-beam assistance.

REFERENCES AND NOTES

1. Mie, G. Beiträge zur Optik Trüber Medien, Speziell Kolloidaler Metallösungen. *Ann. Phys. (Leipzig)* **1908**, *330*, 377.
2. Kreibig, U.; Vollmer, M. *Optical Properties of Metal Clusters*; Springer: Berlin, 1995.
3. Maier, S. A. *Plasmonics: Fundamentals And Applications*; Springer-Verlag: New York, 2007.
4. Maier, S. A.; Atwater, H. A. Plasmonics: Localization and Guiding of Electromagnetic Energy in Metal/Dielectric Structures. *J. Appl. Phys.* **2005**, *98*, 011101.
5. Lee, S. J.; Guan, Z.; Xu, H.; Moskovits, M. Surface-Enhanced Raman Spectroscopy and Nanogeometry: The Plasmonic Origin of SERS. *J. Phys. Chem. C* **2007**, *111*, 17985–17988.
6. Banholzer, M. J.; Millstone, J. E.; Qin, L.; Mirkin, C. A. Rationally Designed Nanostructures for Surface-Enhanced Raman Spectroscopy. *Chem. Soc. Rev.* **2008**, *37*, 885.
7. Le, F.; Brandl, D. W.; Urzhumov, Y. A.; Wang, H.; Kundu, J.; Halas, N. J.; Aizpurua, J.; Nordlander, P. Metallic Nanoparticle Arrays: A Common Substrate for Both Surface-Enhanced Raman Scattering and Surface-Enhanced Infrared Absorption. *ACS Nano* **2008**, *2*, 707–718.

8. Nakayama, K.; Tanabe, K.; Atwater, H. A. Plasmonic Nanoparticle Enhanced Light Absorption in GaAs Solar Cells. *Appl. Phys. Lett.* **2008**, *93*, 121904.
9. Lal, S.; Clare, S. E.; Halas, N. J. Nanoshell-Enabled Photothermal Cancer Therapy: Impending Clinical Impact. *Acc. Chem. Res.* **2008**, *41*, 1842.
10. Lal, S.; Link, S.; Halas, N. J. Nano-optics from Sensing to Waveguiding. *Nat. Photon.* **2008**, *1*, 641.
11. Sönnichsen, C.; Franzl, T.; Wilk, T.; von Plessen, G.; Feldmann, J.; Wilson, O.; Mulvaney, P. Drastic Reduction of Plasmon Damping in Gold Nanorods. *Phys. Rev. Lett.* **2002**, *88*, 077402.
12. Aizpurua, J.; Hanarp, P.; Sutherland, D. S.; Käll, M.; Bryant, G. W.; García de Abajo, F. J. Optical Properties of Gold Nanorings. *Phys. Rev. Lett.* **2003**, *90*, 057401.
13. Hao, F.; Larsson, E. M.; Ali, T. A.; Sutherland, D. S.; Nordlander, P. Shedding Light on Dark Plasmons in Gold Nanorings. *Chem. Phys. Lett.* **2008**, *458*, 262.
14. Wang, H.; Wu, Y.; Lassiter, B.; Nehl, C. L.; Hafner, J. H.; Nordlander, P.; Halas, N. J. Symmetry Breaking in Individual Plasmonic Nanoparticles. *Proc. Natl. Acad. Sci. U.S.A.* **2006**, *103*, 10856–10860.
15. Kumar, P. S.; Pastoriza-Santos, I.; Rodriguez-Gonzalez, B.; de Abajo, F. J. G.; Liz-Marzan, L. M. High-Yield Synthesis and Optical Response of Gold Nanostars. *Nanotechnology* **2008**, *19*, 015606.
16. Sherry, L. J.; Chang, S.-H.; Schatz, G. C.; Duyne, R. P. V.; Wiley, B. J.; Xia, Y. Localized Surface Plasmon Resonance Spectroscopy of Single Silver Nanocubes. *Nano Lett.* **2005**, *5*, 2034–2038.
17. Bergman, D. J.; Stockman, M. I. Surface Plasmon Amplification by Stimulated Emission of Radiation: Quantum Generation of Coherent Surface Plasmons in Nanosystems. *Phys. Rev. Lett.* **2003**, *90*, 027402.
18. Kokkinakis, T.; Alexopoulos, K. Observation of Radiative Decay of Surface Plasmons in Small Silver Particles. *Phys. Rev. Lett.* **1972**, *28*, 1632–1634.
19. Link, S.; El-Sayed, M. A. Shape and Size Dependence of Radiative, Nonradiative and Photothermal Properties of Gold Nanocrystals. *Int. Rev. Phys. Chem.* **2000**, *19*, 409.
20. Meier, M.; Wokaun, A. Enhanced Fields on Large Metal Particles: Dynamic Depolarization. *Opt. Lett.* **1983**, *8*, 581–583.
21. Prodan, E.; Radloff, C.; Halas, N. J.; Nordlander, P. A Hybridization Model for the Plasmon Response of Complex Nanostructures. *Science* **2003**, *302*, 419–422.
22. Hao, F.; Nordlander, P.; Burnett, M. T.; Maier, S. A. Enhanced Tunability and Linewidth Sharpening of Plasmon Resonances in Hybridized Metallic Ring/Disk Nanocavities. *Phys. Rev. B: Condens. Matter Mater. Phys.* **2007**, *76*, 245417.
23. Hao, F.; Sonnefraud, Y.; Van Dorpe, P.; Maier, S. A.; Halas, N. J.; Nordlander, P. Symmetry Breaking in Plasmonic Nanocavities: Subradiant LSPR Sensing and a Tunable Fano Resonance. *Nano Lett.* **2008**, *8*, 3983–3988.
24. Enkrich, C.; Wegener, M.; Linden, S.; Burger, S.; Zschiedrich, L.; Schmidt, F.; Zhou, J. F.; Koschny, T.; Soukoulis, C. M. Magnetic Metamaterials at Telecommunication and Visible Frequencies. *Phys. Rev. Lett.* **2005**, *95*, 203901.
25. Liu, N.; Guo, H.; Fu, L.; Kaiser, S.; Schweizer, H.; Giessen, H. Plasmon Hybridization in Stacked Cut-Wire Metamaterials. *Adv. Mater.* **2007**, *19*, 3628.
26. Christ, A.; Martin, O. J. F.; Ekinci, Y.; Gippius, N. A.; Tikhodeev, S. G. Symmetry Breaking in a Plasmonic Metamaterial at Optical Wavelength. *Nano Lett.* **2008**, *8*, 2171–2175.
27. Liu, N.; Fu, L.; Kaiser, S.; Schweizer, H.; Giessen, H. Plasmonic Building Blocks for Magnetic Molecules in Three-Dimensional Optical Metamaterials. *Adv. Mater.* **2008**, *20*, 3859–3865.
28. Shegai, T.; Li, Z.; Dadosh, T.; Zhang, Z.; Xu, H.; Haran, G. Managing Light Polarization *via* Plasmon−Molecule Interactions Within an Asymmetric Metal Nanoparticle Trimer. *Proc. Natl. Acad. Sci. U.S.A.* **2008**, *105*, 16448–16453.
29. Hao, F.; Nordlander, P.; Sonnefraud, Y.; Van Dorpe, P.; Maier, S. A. Tunability of Subradiant Dipolar and Fano-Type Plasmon Resonances in Metallic Ring/Disk Cavities: Implications for Nanoscale Optical Sensing. *ACS Nano* **2009**, *3*, 643–652.
30. Verellen, N.; Sonnefraud, Y.; Sobhani, H.; Hao, F.; Moshchalkov, V. V.; Van Dorpe, P.; Nordlander, P.; Maier, S. A. Fano Resonances in Individual Coherent Plasmonic Nanocavities. *Nano Lett.* **2009**, *9*, 1663–1667.
31. Pakizeh, T.; Langhammer, C.; Zorić, I.; Apell, P.; Käll, M. Intrinsic Fano Interference of Localized Plasmons in Pd Nanoparticles. *Nano Lett.* **2009**, *9*, 882–886.
32. Li, Z.; Shegai, T.; Haran, G.; Xu, H. Multiple-Particle Nanoantennas for Enormous Enhancement and Polarization Control of Light Emission. *ACS Nano* **2009**, *3*, 637–642.
33. Zhang, S.; Genov, D. A.; Wang, Y.; Liu, M.; Zhang, X. Plasmon-Induced Transparency in Metamaterials. *Phys. Rev. Lett.* **2008**, *101*, 047401.
34. Liu, N.; Langguth, L.; Weiss, T.; Kästel, J.; Fleischhauer, M.; Pfau, T.; Giessen, H. Plasmonic Electromagnetically Induced Transparency at the Drude Damping Limit. *Nat. Mater.* **2009**, *8*, 758–762.
35. Ko, H.; Singamaneni, S.; Tsukruk, V. V. Nanostructured Surfaces and Assemblies as SERS Media. *Small* **2008**, *4*, 1576–1599.
36. Maier, S. A. Plasmonic Field Enhancement and SERS in the Effective Mode Volume Picture. *Opt. Express* **2006**, *14*, 1957–1964.
37. Sherry, L. J.; Jin, R.; Mirkin, C. A.; Schatz, G. C.; Van Duyne, R. P. Localized Surface Plasmon Resonance Spectroscopy of Single Silver Triangular Nanoprisms. *Nano Lett.* **2006**, *6*, 2060–2065.
38. McFarland, A. D.; Van Duyne, R. P. Single Silver Nanoparticles as Real-Time Optical Sensors with Zeptomole Sensitivity. *Nano Lett.* **2003**, *3*, 1057–1062.
39. Liu, N.; Weiss, T.; Mesch, M.; Langguth, L.; Eigenthaler, U.; Hirscher, M.; Sönnichsen, C.; Giessen, H. Planar Metamaterial Analogue of Electromagnetically Induced Transparency for Plasmonic Sensing. *Nano Lett.*, published online September 23, 2009, http://doi.dx.org/10.1021/nl902621d.
40. Hao, F.; Nordlander, P. Efficient Dielectric Function for FDTD Simulation of the Optical Properties of Silver and Gold Nanoparticles. *Chem. Phys. Lett.* **2007**, *446*, 115–118.